

Improved energy storage performance by doping linear dielectrics into lead-free $NaNbO_3$-based ceramics

Yunfeng Guo(郭云凤), Junxian Wang(王俊贤), Xiangkai Zhu(朱香开), Yuxuan Ren(任宇轩), Liming Chen(陈立明), and Jiamao Li(李家茂)

Citation: Chin. Phys. B, 2026, 35 (**2**): 027703. DOI: 10.1088/1674-1056/adefd8
http://cpb.iphy.ac.cn; http://iopscience.iop.org/cpb

What follows is a list of articles you may be interested in

Electrocaloric refrigeration: From physical fundamentals to practical devices

Feiyu Zhang(张费宇), Tiannan Yang(杨天南), and Xiaoshi Qian(钱小石)
Chin. Phys. B, 2026, 35 (**2**): 027701. DOI: 10.1088/1674-1056/ae1f80

Improved ferroelectricity in Mn-doped HfO_2 (111) epitaxial thin films through controlled doping and substrate orientation

Jiayi Gu(顾嘉仪), Haiyi Zhang(张海义), Weijin Pan(潘炜进), Haifeng Bu(卜海峰), Zhijian Shen(沈志健), Shengchun Shen(沈胜春), Yuewei Yin(殷月伟), and Xiaoguang Li(李晓光)
Chin. Phys. B, 2025, 34 (**8**): 087701. DOI: 10.1088/1674-1056/add1bc

Positive and negative electrocaloric effects

Hongrui Xu(徐洪瑞) and Jiping Huang(黄吉平)
Chin. Phys. B, 2025, 34 (**6**): 067702. DOI: 10.1088/1674-1056/adc36c

High-performance KNN-based piezoelectric ceramics for buzzer application

Cheng Xiong(熊城), Bosen Li(李博森), Zhongxin Liao(廖忠新), Yan Qiu(邱奘), and Daqiang Gao(高大强)
Chin. Phys. B, 2025, 34 (**4**): 047701. DOI: 10.1088/1674-1056/adb25e

Efficiently enhanced energy storage performance of $Ba_2Bi_4Ti_5O_{18}$ film by co-doping Fe^{3+} and Ta^{5+} ion with larger radius

Qiong Wu(吴琼), Lei Zhao(赵雷), Xinghao Chen(陈兴豪), and Shifeng Zhao(赵世峰)†
Chin. Phys. B, 2022, 31 (**9**): 097701. DOI: 10.1088/1674-1056/ac5393

Improved energy storage performance by doping linear dielectrics into lead-free $NaNbO_3$-based ceramics

Yunfeng Guo(郭云凤), Junxian Wang(王俊贤), Xiangkai Zhu(朱香开),
Yuxuan Ren(任宇轩), Liming Chen(陈立明), and Jiamao Li(李家茂)†

Advanced Ceramics Research Center, School of Materials Science and Engineering, Anhui University of Technology, Ma'anshan 243032, *China*

(Received 24 April 2025; revised manuscript received 15 June 2025; accepted manuscript online 15 July 2025)

$NaNbO_3$-based lead-free dielectric ceramics possess significant application prospects in the field of dielectric capacitors. However, their development is hindered by low recoverable energy storage density (W_{rec}) and energy storage efficiency (η). Herein, novel $NaNbO_3$-based ceramics, $(1-x)$ [$0.7Na_{0.97}Sm_{0.01}NbO_3$–$0.3(Sr_{0.7}Bi_{0.2})(Ti_{0.8}Zr_{0.2})O_3$]–$xCaTiO_3$, were created by adding $CaTiO_3$ linear dielectric, aiming to improve their energy storage performance (ESP). The phase structure, microstructure, dielectric properties, energy storage and charge–discharge performances of the ceramics were methodically analyzed. All components of the ceramics exhibit a perovskite structure consisting of two phases: antiferroelectric *P*-phase (AFE *P*) and antiferroelectric *R*-phase (AFE *R*), with the AFE *R* phase increasing as *x* rises. All ceramic surfaces exhibit clear grain morphology. The resultant ceramics have an appropriate dielectric constant and a small dielectric loss, which are beneficial for improving breakdown field strength (E_b). Finally, at an E_b of 470 kV/cm, 0.85[$0.7Na_{0.97}Sm_{0.01}NbO_3$–$0.3(Sr_{0.7}Bi_{0.2})(Ti_{0.8}Zr_{0.2})O_3$]– $0.15CaTiO_3$ ceramic achieves optimal ESP: $W_{rec} = 3.9$ J/cm^3, $\eta = 72.49\%$. In addition, it has remarkable stability with temperature and frequency in energy storage and displays ultrafast speed in the charge–discharge process ($t_{0.9} = 27$ ns).

Keywords: $NaNbO_3$, linear dielectric, energy storage performance, charge–discharge rate

PACS: 77.84.–s, 77.22.–d

DOI: 10.1088/1674-1056/adefd8 **CSTR:** 32038.14.CPB.adefd8

1. Introduction

With the advancement of the electronics industry, the requirements for electronic materials are also increasing. Ceramics for lead-free dielectric energy storage have gained popularity as high-power density energy storage materials.[1–3] Various types of lead-free linear dielectric materials, ferroelectric materials, relaxor ferroelectric materials and antiferroelectric materials have been reported successively.[4,5] Recently, as electronic devices have been evolving towards miniaturization, integration and lightweight design, the demand for higher-performance energy storage components has been growing significantly. The high energy storage density of $NaNbO_3$ (NN)-based relaxor ferroelectric ceramics enables them to store more energy in a smaller volume, which is beneficial for miniaturizing and enhancing the performance of electronic devices.[6–8] They can be applied to power management modules in portable electronic devices such as smartphones, tablets and laptops.

The following formulas can be used to determine the dielectric capacitors' energy storage density and efficiency:[9,10]

$$W_{total} = \int_0^{P_m} E\,\mathrm{d}P, \tag{1}$$

$$W_{rec} = \int_{P_r}^{P_m} E\,\mathrm{d}P, \tag{2}$$

$$\eta = \frac{W_{rec}}{W_{total}} \times 100\%. \tag{3}$$

Among them, W_{total}, P_m, P_r, W_{rec}, E and η represent total energy storage density, saturation polarization, residual polarization, recoverable energy storage density, electric field and efficiency, respectively.

The hysteresis loop of NN-based ceramics exhibits a square ferroelectric phase hysteresis loop, with significant residual polarization and limited energy storage performance (ESP). The polarization strength of linear dielectrics exhibits a linear relationship with the applied electric field, without hysteresis, thus achieving high energy storage efficiency.[11] Compared to the other types of ceramic capacitors, many linear dielectrics typically have a higher E_b.[12,13] However, extremely low polarization strength and dielectric constant severely limit their application in energy storage.[14–16] Therefore, by combining NN-based ceramics and linear dielectrics, the breakdown strength can be improved, residual polarization can be reduced and thus ESP can be enhanced. For instance, Feng *et al.*[17] added $SrTiO_3$ (a linear perovskite material) into $0.76NaNbO_3$–$0.24(Bi_{0.5}Na_{0.5})TiO_3$ ceramics. At a 270 kV/cm of E_b, a W_{rec} of 2.64 J/cm^3 and an ultra-high η of 89.9% were achieved. Kang *et al.*[18] investigated that the $NaNbO_3$–$Bi(Zn_{0.5}Sn_{0.5})O_3$ added a linear dielectric material $SrTiO_3$ (the added amount is 0.192), exhibited a W_{rec} of 5.82 J/cm^3 and a η of 92.3%.[19]

†Corresponding author. E-mail: lijiamao@ahut.edu.cn

© 2026 Chinese Physical Society and IOP Publishing Ltd. All rights, including for text and data mining, AI training, and similar technologies, are reserved.

In comparison to $SrTiO_3$, $CaTiO_3$ (CT) has a high dielectric strength (300 kV/cm) and a low dielectric loss ($\sim 10^{-5}$).[20] In addition, its reported large band gap and dielectric constant are about 3.4 eV and 175, respectively.[21] These physical properties indicate that CT is a promising dielectric for enhancing the ESP of $NaNbO_3$-based ceramics. Chen *et al.*[22] designed a $(1-x)(0.92NaNbO_3$–$0.08Bi(Mg_{0.5}Ti_{0.5})O_3)$–$xCaTiO_3$ ceramic system, achieving a W_{rec} of 5.71 J/cm^3 at 475 kV/cm with a 20% addition of CT. Zhang *et al.*[23] acquired a high W_{rec} of 6.84 J/cm^3 in $0.6(0.96NaNbO_3$–$0.04BiFeO_3)$–$0.4CaTiO_3$. In our preliminary research, we obtained an W_{rec} of 3.2 J/cm^3 in $0.7Na_{1-3x}Sm_xNbO_3$–$0.3(Sr_{0.7}Bi_{0.2})(Ti_{0.8}Zr_{0.2})O_3$ (abbreviated as xSm) ceramics, but its η was below 70%.[24] Therefore, by adding linear dielectric CT into $0.7Na_{1-3x}Sm_xNbO_3$–$0.3(Sr_{0.7}Bi_{0.2})(Ti_{0.8}Zr_{0.2})O_3$, we aim to improve its energy storage efficiency, which has never been studied.

2. Experimental details

The traditional solid-state sintering method was used to prepare $(1-x)[0.7Na_{0.97}Sm_{0.01}NbO_3$–$0.3(Sr_{0.7}Bi_{0.2})(Ti_{0.8}Zr_{0.2})O_3]$–$xCaTiO_3$ [abbreviated as xCT, $x = 0.06$, 0.09, 0.12, 0.15] ceramics. Sodium carbonate (Na_2CO_3, 99.8%), strontium carbonate ($SrCO_3$, 99%), niobium pentoxide (Nb_2O_5, 99.9%), bismuth trioxide (Bi_2O_3, 99.8%), titanium dioxide (TiO_2, 99%), zirconium dioxide (ZrO_2, 99%), calcium carbonate ($CaCO_3$, 99%) and samarium oxide (Sm_2O_3, 99.99%) were weighed in stoichiometric proportions and placed in a nylon ball mill jar. Zirconia balls were used as ball milling media and the mixture was subjected to ball milling with anhydrous ethanol for a duration of 8 h. Following the drying of the slurry, it was then calcined for 3 h at 950 °C in a muffle furnace. The resultant powder underwent a second ball milling for an additional 8 h. After drying, polyvinyl alcohol (PVA) was incorporated and the mixture was sieved through an 80 mesh sieve. The resulting product was compressed into a cylindrical green body at 200 MPa, and PVA was discharged at 600 °C for 2 h prior to sintering at 1240 °C–1300 °C for 2 h. Finally, the ceramic samples were polished to a thickness of approximately 0.1 mm, and then silver electrodes were applied to the surface to measure electrical performance.

Using the Archimedes method, the bulk density (ρ_{bu}) of the ceramics was determined. The relative density (ρ_{re}) was calculated as follows:

$$\rho_{re} = \frac{\rho_{bu}}{\rho_{th}} \times 100\%, \tag{4}$$

where ρ_{th} was the theoretical density and was obtained by the Rietveld refinement method. The phase structure of ceramic samples was investigated by x-ray diffraction (XRD, Ultima IV, Rigaku) and Raman spectroscopy (Raman, inVia Qontor, Renishaw). The microstructure was investigated through field-emission scanning electron microscopy (SEM, MIRA3, TESCAN), and the grain size was measured by means of Nano Measurer software. The dielectric performances were measured by a precision impedance analyzer (Impedance Analyzer E4990A, Keysight) in the temperature range of room temperature to 500 °C. The hysteresis loop (P–E) was tested via a ferroelectric testing system (TF Analyzer 2000 E, aixACCT). The charge–discharge performance was tested by a dielectric charge–discharge testing system (CFD-003).

3. Results and discussion

The XRD patterns of xCT ceramics and the magnified (200) diffraction peaks are displayed in Fig. 1. As illustrated in Fig. 1(a), all ceramic components have a perovskite structure and no impurity phases are observed in the scanning range. This result indicates that CT has effectively infiltrated the NN lattice to form a solid solution. Figure 1(b) demonstrates that as the CT content rises, the diffraction peaks progressively shift towards higher angles, a phenomenon attributed to the lattice contraction of the ceramic, which results in a reduction of the unit cell volume. This is because the smaller ionic radius Ca^{2+} (1.34 Å, CN = 12) replaces the larger ionic radius Na^+ (1.39 Å, CN = 12), Bi^{3+} (1.36 Å, CN = 12) and Sr^{2+} (1.44 Å, CN = 12). The (200) diffraction peaks of the ceramics split, showing a higher left side and a lower right side, demonstrating that the phase structure is orthorhombic.[25] The specific phase structure was determined by XRD Rietveld refinement.

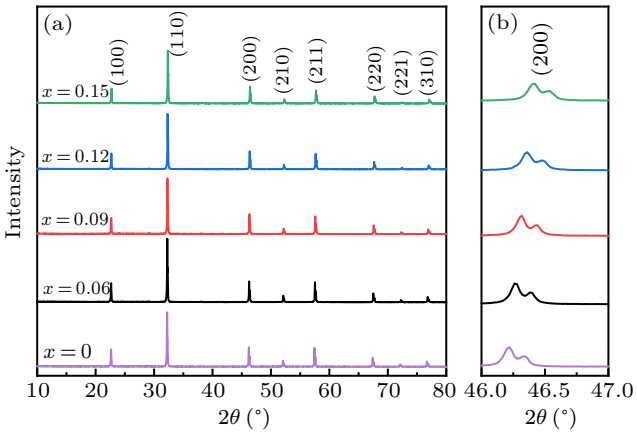


Fig. 1. (a) XRD patterns of xCT ceramics; (b) amplification peak at 46°–47°.

In order to precisely characterize the changes in phase structure, GSAG software was used to fit the XRD data. Figure 2 indicates the refined patterns. Table 1 shows the refined parameters after fitting. The R_{wp} and R_p of all components are below 10%, and χ^2 is between 1.370 and 1.569, demonstrating the reliability of Rietveld fitting. Moreover, the addition of CT significantly increases the content of AFE R phase, manifesting that CT is beneficial for improving the stability of AFE R

phase. As the CT content increases, the *R* phase content gradually increases and remains predominant. However, the phase structure of the coexistence of AFE *P* and AFE *R* phases still exists in the *x*CT ceramics. In addition, the volume of the crystal cell gradually decreases, corroborating the previous XRD analysis results.

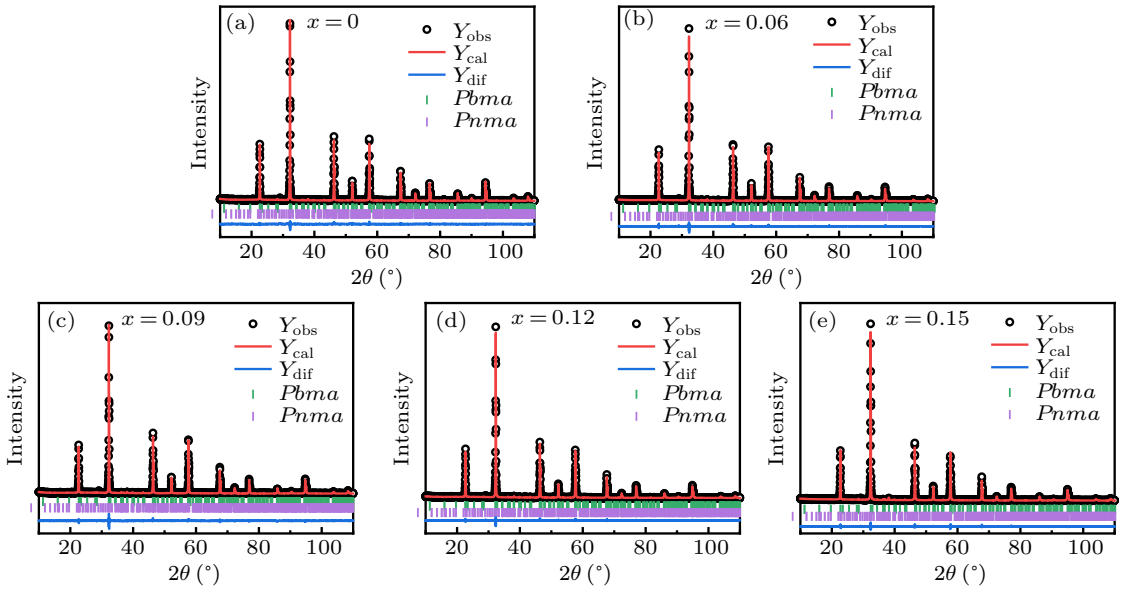


Fig. 2. Rietveld refinement patterns of *x*CT ceramics.

Table 1. Refined structural parameters of *x*CT ceramics.

x	Phase structure	Phase content (wt%)	Lattice parameters				Cell volume (Å^3)	*R* factors		
			a (Å)	*b* (Å)	*c* (Å)	$\alpha = \beta = \gamma$ (°)		R_{wp} (%)	R_p (%)	χ^2
0.0	*Pbma*	40.26	5.56(9)	15.68(1)	5.53(6)	90	485.34(6)	8.22	6.49	1.176
	Pnma	59.74	7.85(6)	7.85(4)	23.55(8)	90	1453.44(4)			
0.06	*Pbma*	37.76	5.56(0)	15.65(6)	5.54(4)	90	482.73(2)	8.49	6.76	1.548
	Pnma	62.24	7.84(0)	7.84(0)	23.51(0)	90	1445.39(5)			
0.09	*Pbma*	35.61	5.55(6)	15.64(3)	5.54(2)	90	481.77(0)	8.71	6.85	1.540
	Pnma	64.38	7.83(3)	7.83(0)	23.49(9)	90	1441.59(5)			
0.12	*Pbma*	29.65	5.55(2)	15.64(3)	5.54(3)	90	481.46(9)	8.27	6.50	1.370
	Pnma	70.35	7.82(6)	7.82(7)	23.46(8)	90	1437.76(4)			
0.15	*Pbma*	28.08	5.52(9)	15.63(9)	5.53(0)	90	478.23(1)	8.83	6.81	1.569
	Pnma	71.92	7.81(8)	7.81(7)	23.45(3)	90	1433.45(5)			

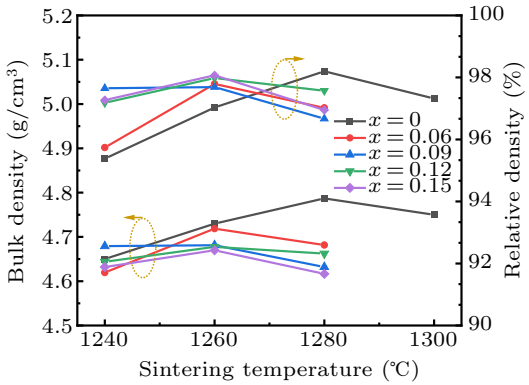


Fig. 3. Bulk density and relative density of *x*CT ceramics sintered at different temperatures.

The density profiles of *x*CT ceramics are demonstrated in Fig. 3. All density curves initially experience a rise followed by a decline along with sintering temperature changes. High density ($> 97.5\%$) is beneficial for improving dielectric and energy storage properties.

Figure 4 displays the Raman spectra of $0.7NaNbO_3$–$0.3(Sr_{0.7}Bi_{0.2})(Ti_{0.8}Zr_{0.2})O_3$ [abbreviated as NN-SBTZ] and *x*CT ceramics, as well as the Gaussian–Lorentz function fitting curve at $x = 0.06$ (fitted using PeakFit software). In Fig. 4(a), as *x* increases, there is no significant change in the number of Raman peaks, implying that the phase structure of the ceramics remains stable. However, the peaks between 220 cm^{-1} and 600 cm^{-1} exhibit a gradual widening and flattening. This phenomenon is due to the enhancement of structural disorder and the weakening of cell polarity.[26] Compared with NN-SBTZ, the Raman curve of *x*CT ceramic shows the same trend before 700 cm^{-1}, but there is an additional Raman peak at 1100 cm^{-1}. One possible reason for this behavior is that the substitution of Sm^{3+} (1.24 Å) for Na^+ (1.39 Å) in $NaNbO_3$ can cause lattice contraction, resulting in shortened Nb–O bond length, enhanced bond energy, and a shift in vibration frequency towards higher wave numbers.[27,28] As a result, an

additional Raman peak appears at 1100 cm^{-1}.

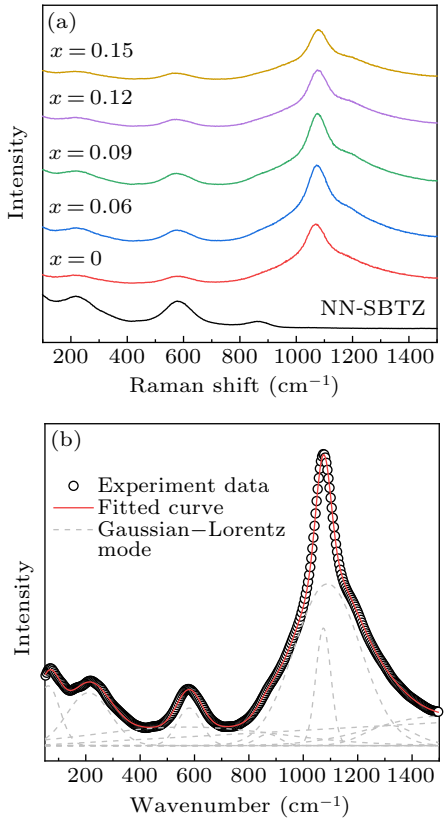


Fig. 4. (a) Raman spectra of *x*CT ceramics and NN-SBTZ ceramic; (b) fitting curve of Gaussian–Lorentz model at $x = 0.06$.

Figure 5 shows the SEM images and relevant grain size distribution of *x*CT ceramics. The ceramic grains of all components are clearly visible, with distinct grain boundaries and no obvious pores. These findings imply that *x*CT ceramics, which are sintered at 1260 °C, possess a high density, a characteristic that is advantageous for enhancing ferroelectric properties. This is consistent with the test results in Fig. 3. The average grain sizes, as depicted in Figs. 5(a)–5(d), are measured as 3.78 μm, 3.35 μm, 3.28 μm and 3.21 μm for the samples with *x* values ranging from 0.06 to 0.15, respectively. Clearly, the average grain size of ceramics demonstrates a consistent decreasing trend. With the introduction of CT, the content of Bi gradually decreases. This decline in Bi concentration correlates with a decrease in the presence of oxygen vacancies, which subsequently inhibits the migration of grain boundaries and the growth of grains. Furthermore, this phenomenon may be attributed to the stochastic distribution of diverse A-site cations (Na^+, Sm^{3+}, Sr^{2+}, Bi^{3+} and Ca^{2+}), which contributes to an increase in lattice strain energy and further suppresses grain growth.[29] A smaller grain size is conducive to achieving high breakdown strength and improving W_{rec}.[30] In addition, the grain sizes of *x*CT ceramics are not uniform, as displayed in Fig. 5. This is because the ionic radius of Sm^{3+} (1.24 Å, CN = 12) is smaller than that of Na^+ (1.39 Å, CN = 12). When Sm^{3+} is doped into $NaNbO_3$, lattice distortion will be generated. Different degrees of local distortion may lead to a difference in diffusion rate, which in turn affects the grain growth rate. Figure 6 presents the energy dispersive spectroscopy (EDS) spectrum of 0.15CT ceramic, indicating a uniform distribution of elements, with their proportions aligning with theoretical values. This uniformity is advantageous for enhancing ESP.

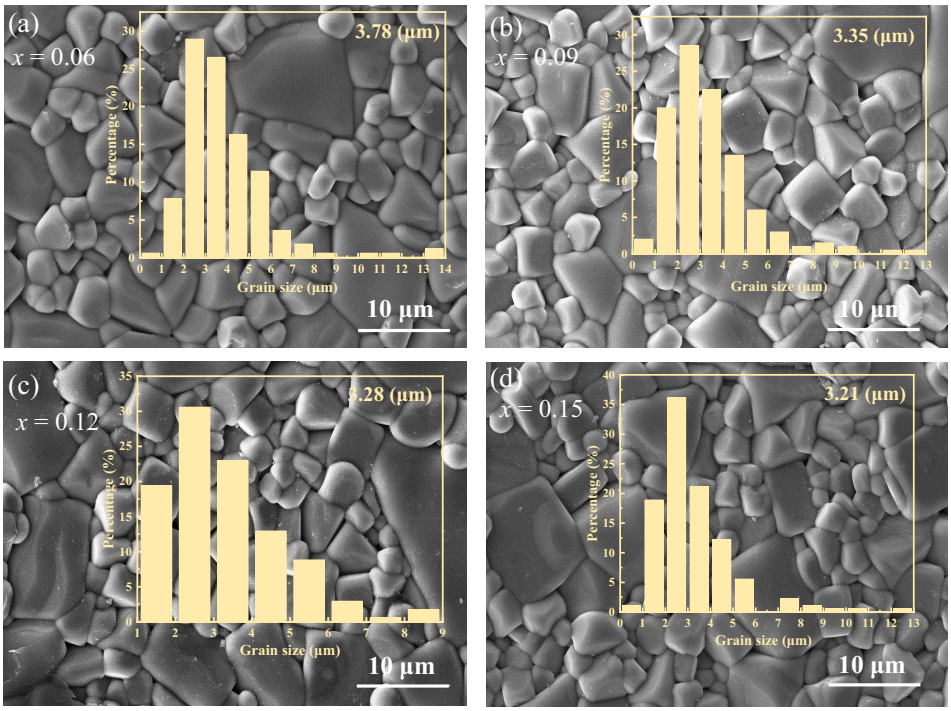


Fig. 5. SEM images of *x*CT ceramics and related grain size distribution.

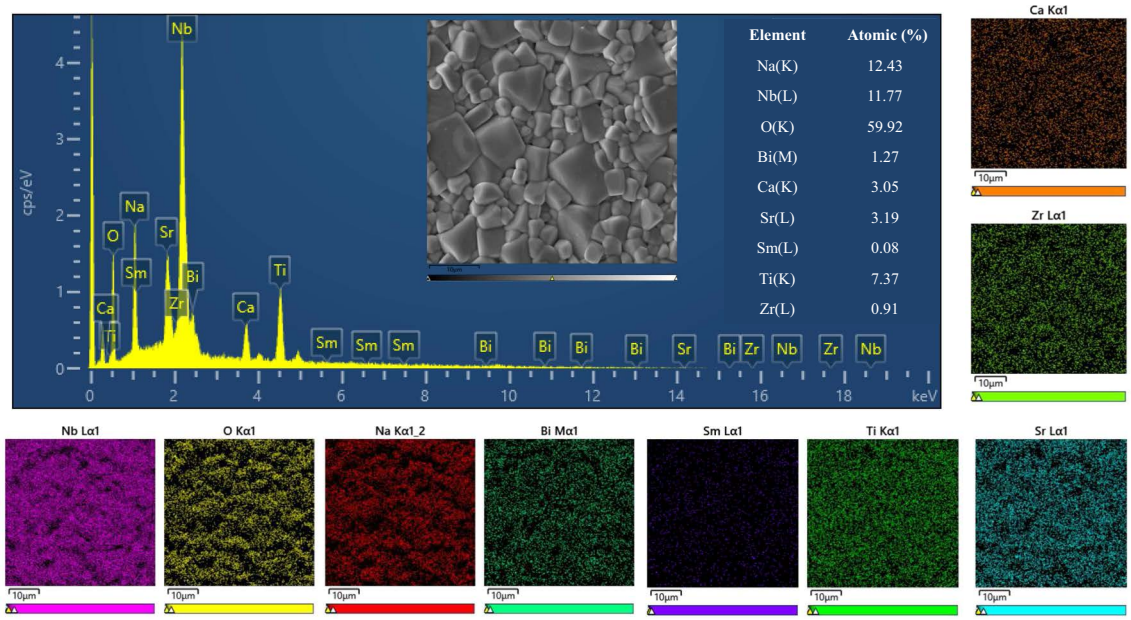


Fig. 6. EDS spectrum and elemental distribution maps of 0.15CT ceramic.

Figure 7 illustrates the temperature-dependent dielectric constant (ε_r) and dielectric loss ($\tan\delta$) of xCT ceramics across various frequencies (1 kHz to 1 MHz). The ε_r of the ceramic gradually decreases with rising temperature, and no phase transition peak appears in any of the components. This means that xCT ceramics are mainly in the R phase at room temperature, with the phase transition point having dropped below room temperature.[31] None of the components exhibit a change in phase structure, and they are all coexisting two-phase structures, which is consistent with the previously mentioned XRD refinement results and Raman spectroscopy analysis results. As x increases, the ε_r gradually decreases. A larger ε_r will reduce the E_b of the ceramic, while a smaller ε_r will reduce the P_m of the ceramic. Therefore, this ceramic component of $x = 0.15$ is advantageous for obtaining higher W_{rec} due to its moderate ε_r. At temperatures above 350 °C, an increase in frequency for all ceramic compositions correlates with a decrease in $\tan\delta$. Furthermore, the $\tan\delta$ of ceramics decreases as the doping amount increases at room temperature. Moreover, all the $\tan\delta$ values at room temperature are below 1%. When $x = 0.15$, the dielectric loss of ceramics is the smallest, as shown in Fig. 7(e). Low $\tan\delta$ is conducive to reducing energy loss and increasing η.

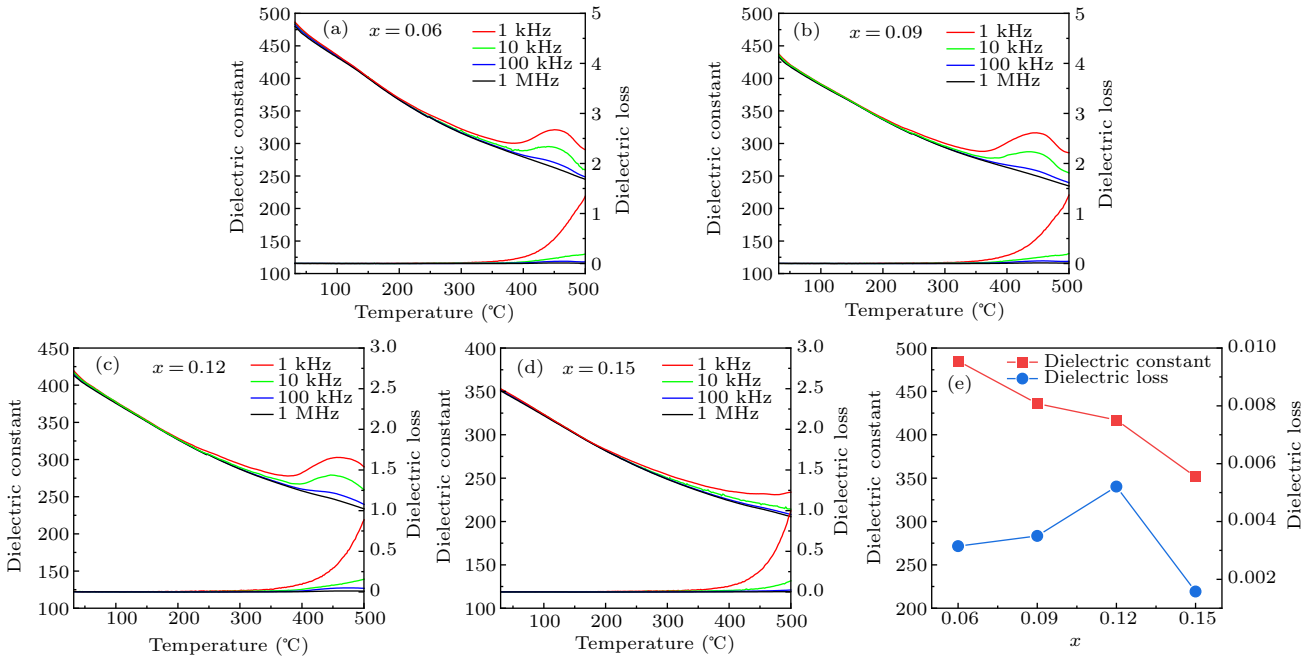


Fig. 7. (a)–(d) Correlations between ε_r and $\tan\delta$ of xCT ceramics and temperature at various frequencies; (e) ε_r and $\tan\delta$ of xCT ceramics at room temperature at 10 kHz.

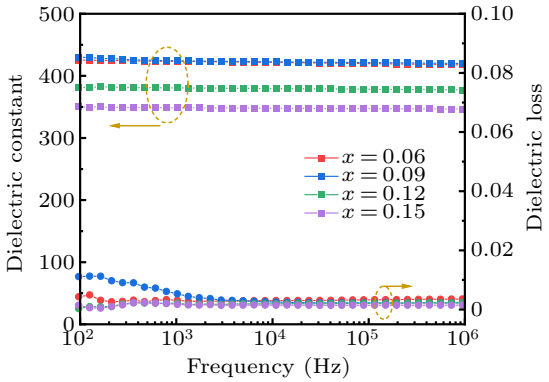


Fig. 8. ε_r and $\tan\delta$ of xCT ceramics at different frequencies.

Figure 8 displays the ε_r and $\tan\delta$ values for xCT ceramics tested at different frequencies. As x increases, the ε_r shows a decreasing trend. This is because the low polarized ion Ca^{2+} (polarization rate: $Ca^{2+} = 3.16 \times 10^{-3}$ nm^3, $Sm^{3+} = 4.74 \times 10^{-3}$ nm^3, $Sr^{2+} = 4.25 \times 10^{-3}$ nm^3, $Bi^{3+} = 6.12 \times 10^{-3}$ nm^3) reduces the polarization of A-site, and the polarity of B-site ions cannot compensate for the loss of A-site ion polarity, leading to a decline in ε_r. With the increase in frequency, the ε_r of ceramics remains basically unchanged. A medium dielectric constant can achieve high P_m and E_b values. When $x = 0.15$, it has an ultra-low $\tan\delta$ (< 0.005), which is beneficial for reducing heat and achieving superior stability and high E_b value.

Figures 9(a)–9(c) show the unipolar polarization–electric field (P–E) loops of xCT ceramics at room temperature, as well as the corresponding variations of P_m, P_r, ΔP, W_{rec} and η with x. At $x = 0.15$, the ceramic demonstrates optimal ESP: $W_{rec} = 3.9$ J/cm^3, $\eta = 72.49\%$. Compared with the performance of 0CT ceramic ($W_{rec} = 3.2$ J/cm^3, $\eta = 69\%$), both W_{rec} and η are improved simultaneously when CT is added to the matrix, meeting the requirement of improving energy storage efficiency with linear dielectrics. The E_b is recognized as the critical determinant of ESP. To assess the E_b of xCT ceramics, the Weibull distribution analysis was employed, as depicted in Fig. 9(d). The relevant calculation formulas are provided as follows:[32,33]

$$X_i = \mathrm{Ln}(E_i), \tag{5}$$

$$Y_i = \mathrm{Ln}\left(\mathrm{Ln}\left(1\Big/\left(1-\frac{i}{i+n}\right)\right)\right), \tag{6}$$

where X_i and Y_i represent variables in the Weibull expression, E_i denotes the breakdown strength, i represents the ordinal number and n signifies the total sample size ($n = 8$). The components of the Weibull index ($\beta \geq 10$) have a linear relationship, indicating excellent reliability of Weibull distribution analysis.[34] Figure 9(d) shows that the breakdown strength reaches its maximum value at $x = 0.15$.

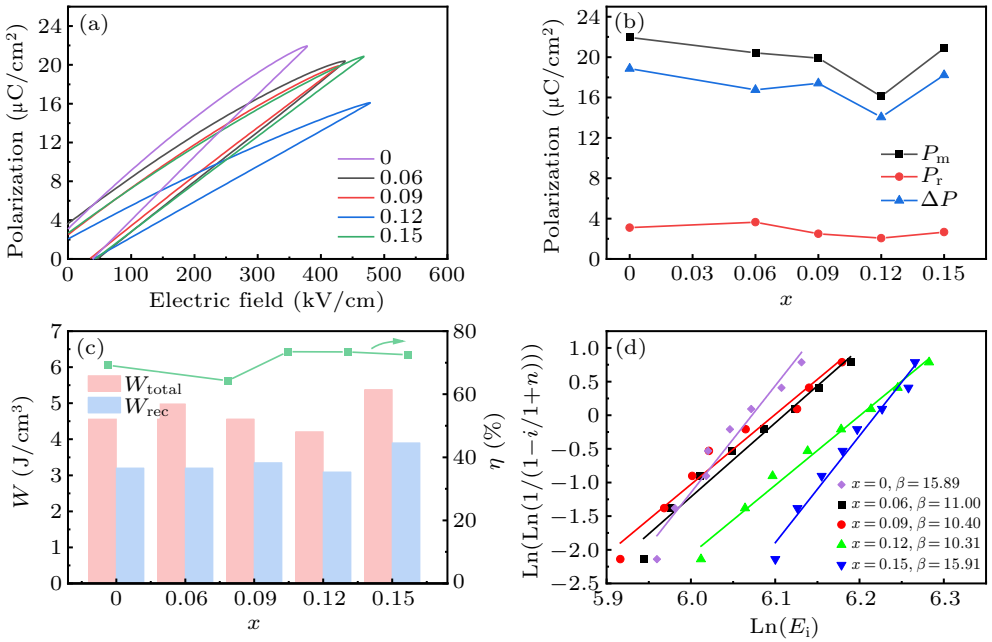


Fig. 9. (a) Unipolar P–E loop, (b), (c) ESP of xCT ceramics at different electric fields and (d) related Weibull distribution.

Figure 10 illustrates the unipolar P–E loops of 0.15CT ceramic under varying electric fields, as well as the corresponding changes in P_m, P_r, ΔP, W_{rec} and η. When the electric field increases to 470 kV/cm, P_m linearly increases to 20.89 μC/cm^2, while P_r slowly increases to 2.66 μC/cm^2, which also leads to a decrease in efficiency. Notably, P_m exhibits a significantly higher growth rate compared to P_r. This implies that as the electric field intensifies, the value of ΔP expands. Consequently, the change in W_{rec} is consistent with ΔP, with W_{rec} escalating to 3.9 J/cm^3. However, the η declines slightly from 83.44% to 72.49%. This decrease in η is attributed to energy loss, which arises from the intensive resid-

ual polarization with the increase in electric field. One can deduce that for applications in high-electric-field environments, the optimal component should reduce residual polarization to achieve high η.

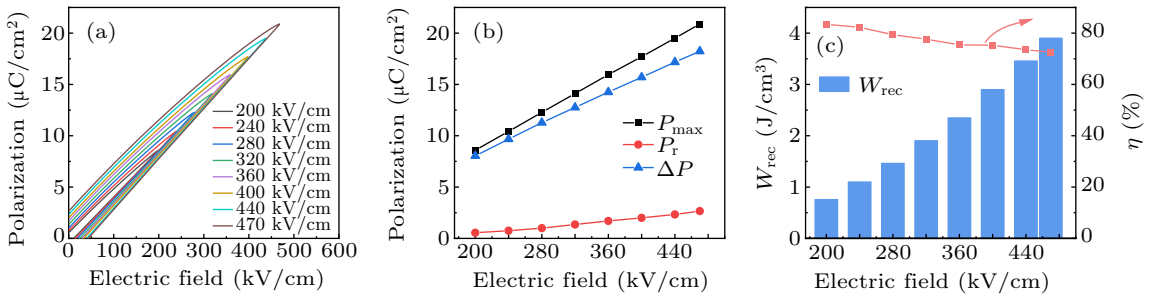


Fig. 10. (a) *P*–*E* loop and (b), (c) ESP of 0.15CT ceramic at different electric fields.

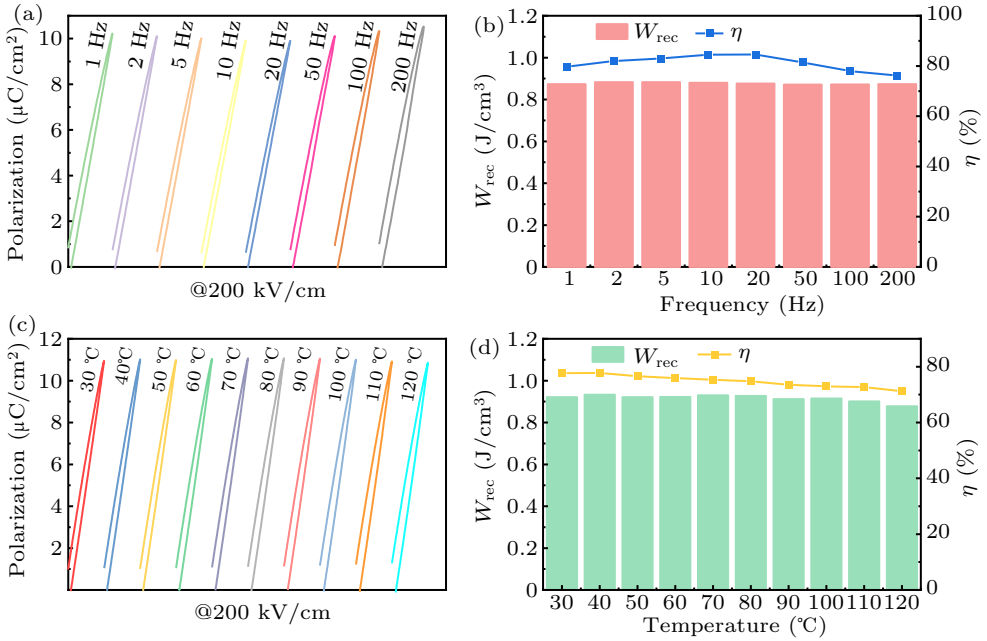


Fig. 11. (a) *P*–*E* loops of 0.15CT ceramic under diverse frequencies and (b) relevant W_{rec} and η; (c) *P*–*E* loops of 0.15CT ceramic under diverse temperatures and (d) relevant W_{rec} and η.

The excellent temperature/frequency stability of dielectric performance is a crucial parameter for maintaining the operational stability of ceramic capacitors. Figures 11(a)–11(c) illustrate the temperature/frequency-dependent unipolar *P*–*E* loops of 0.15CT ceramic at 200 kV/cm. Meanwhile, the relevant ESP, derived from Eqs. (1)–(3), is presented in Figs. 11(b) and 11(d), respectively. All samples exhibit slender *P*–*E* loops when measuring temperature and frequency. From Fig. 11(b), it can be observed that the increase in frequency has little effect on W_{rec}, with a change rate of only 0.5% to 0.7%, and has little effect on η, with a change rate of 3.38% to 5%. This analysis suggests that the ESP of 0.15CT ceramics is dependent on the stability of frequency ($W_{rec} = 0.876 \pm 0.005$ J/cm^3, $\eta = 81.17\% \pm 3.02\%$). Similarly, from Fig. 11(d), the variation in amplitude of W_{rec} is very small within a wide temperature range (30 °C–120 °C), and the calculated change rate is only between 1.7% and 3.8%, with a slight decrease in η and a change rate between 2.5% and 3.64%. Therefore, the ESP of 0.15CT ceramic is temperature stable ($W_{rec} = 0.916 \pm 0.016$ J/cm^3, $\eta = 74.84\% \pm 2.22\%$).

The underdamped and overdamped discharge current curves of 0.15CT ceramic at varying electric fields were characterized to identify its actual charge–discharge capacity. Current density (C_D), power density (P_D) and discharge energy density (W_d) are key performance parameters of capacitors in pulse charge–discharge performance, and the calculation formulas are as follows:[28,35]

$$C_D = \frac{I_{max}}{S}, \tag{7}$$

$$P_D = \frac{EI_{max}}{2S}, \tag{8}$$

$$W_d = \frac{R\int i^2(t)\,dt}{V}, \tag{9}$$

where I_{max} represents the peak current, E stands for the magnitude of the electric field, S indicates the surface area of the silver electrode, R represents the load resistance and V represents the volume of the test sample. The fast charge–discharge

characteristics of dielectric energy storage ceramics are also reflected in their short charge–discharge time. Short charge–discharge time means that ceramics can complete the charge–discharge process in a very short time, meeting the demand for fast response, represented by $t_{0.9}$ (the value numerically corresponds to the discharge time at which W_d reaches 90% of its saturated state).

As depicted in Fig. 12(a), the peak current exhibits an increase with the electric field. At 12 kV/mm, the maximum discharge peak current is 10.25 A. As shown in Fig. 12(b), I_{max}, C_D and P_D at different electric fields show the same trend, steadily increasing with increasing electric field. I_{max}, C_D and P_D at 12 kV/mm reach 10.26 A, 326.4 A/cm^2 and 39.17 MW/cm^3, respectively. The overdamped discharge current of $R = 200.5$ Ω under varying electric fields is presented in Figs. 12(c) and 12(d). As the electric field intensifies, W_d increases to 0.8 J/cm^3, with a charge–discharge rate of 27 ns, indicating superior charge–discharge speed relative to other studies.[24,29,35–40] This high charge–discharge rate renders the material particularly suitable for high-power and pulse power applications, including hybrid electric vehicles, medical defibrillators, spacecraft, satellites and electric weapon systems.

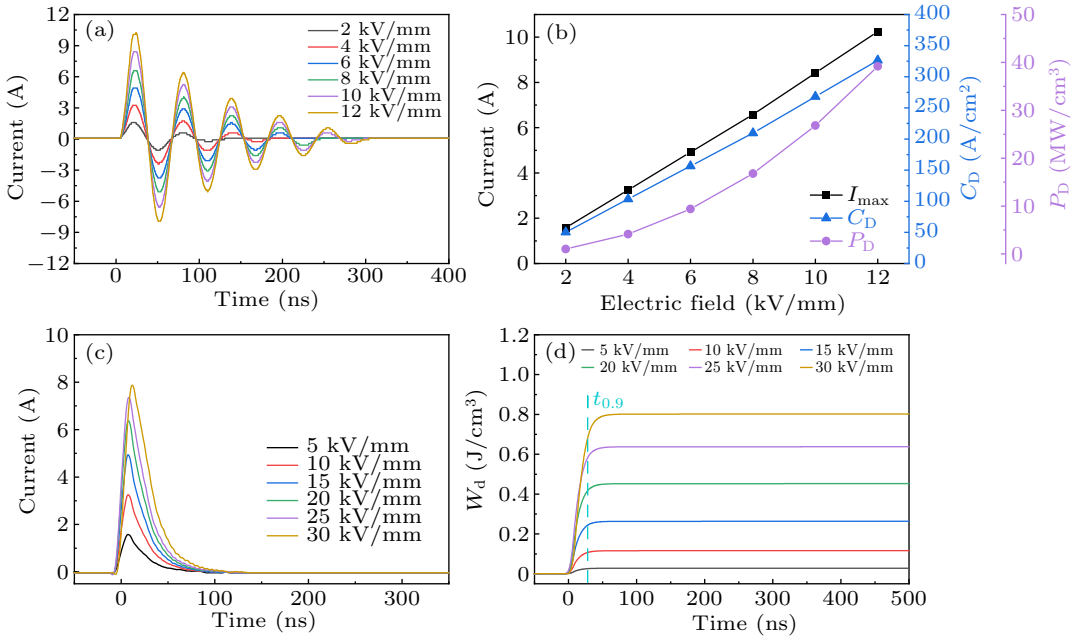


Fig. 12. (a) Charge–discharge current curves with the underdamped characteristic of 0.15CT ceramic and (b) relevant I_{max}, C_D and P_D; (c) charge–discharge current curves with the overdamped characteristic of 0.15CT ceramic and (d) the relevant W_d.

4. Conclusion

In this paper, xCT ceramics were prepared using the traditional solid-state reaction approach. The phase structure, microstructure, dielectric properties, energy storage and charge–discharge of ceramics were characterized. At an E_b of 470 kV/cm, 0.15CT ceramic achieves optimal ESP: $W_{rec} = 3.9$ J/cm^3, $\eta = 72.49\%$. Compared with 0.01Sm, E_b is significantly improved, ESP is enhanced and efficiency is promoted, meeting the requirements of using linear dielectrics to increase rates. In addition, 0.15CT ceramic also exhibits a P_D of 39.17 MW/cm^3, a C_D of 326.4 A/cm^2 and an extremely rapid charge–discharge rate, reaching 27 ns. The charge–discharge performance of this material surpasses that of 0.01Sm. Based on the above results, 0.15CT ceramic is a potential energy storage capacitor.

Acknowledgement

Project supported by the Natural Science Foundation of Anhui Provincial Education Department (Grant No. KJ2019A0054).

References

[1] Yao J K and Zhong W S 2023 *Chin. Phys. B* **32** 018101
[2] Dan Y J, Tang LP, Ning W Z, Meng Y Z, Hu C Z, Liu L J and Fang L 2024 *J. Adv. Ceram.* **13** 1349
[3] Guo Y F, Wang J X, Wang Z X, Li J M and Chen L M 2025 *Acta Phys. Sin.* **74** 017702 (in Chinese)
[4] Zhou L, Zhang X L, Cao Y Y, Zheng F, Gao H, Liu H F and Ma Z 2023 *Chin. Phys. B* **32** 017701
[5] Fan X H, Wang J, Yuan H, Zheng Z H, Zhang J and Zhu K J 2023 *J. Adv. Ceram.* **12** 649
[6] Zhang L, Chen Z G, Luo G G, Aid F R and Luo N N 2023 *J. Eur. Ceram. Soc.* **43** 6077
[7] Bi W J, Li L M, Tian G, Hao J G, Zhai X, Bai H R, Du J, Chen C, Li W and Zheng L M 2023 *Chem. Eng. J.* **478** 147383
[8] Guo Y Q, Jain A, Zhou H Z and Wang Y G 2024 *Ceram. Int.* **50** 50038
[9] Dai S W, Li M Y, Wu X W, Wu Y Y, Li X, Hao Y N and Luo B C 2024 *J. Adv. Ceram.* **13** 877
[10] Guo Y F, Wang J X, Wang Z X, Li J M and Liu C 2024 *Acta Chim. Sin.* **82** 511
[11] Jayakrishnan A R, Silva J P B, Kamakshi K, Dastan D, Annapureddy V, Pereira M and Sekhar K C 2023 *Prog. Mater. Sci.* **132** 101046
[12] Pu Y P, Wang W, Guo X, Shi R K, Yang M D and Li J W 2019 *J. Mater. Chem. C* **7** 14384

[13] Zhang J W, Wang J, Gao D D, Liu H, Xie J Y and Hu W B 2021 *J. Eur. Ceram. Soc.* **41** 352
[14] Zhou H Y, Zhu X N, Ren G R and Chen X M 2016 *J. Alloys Compd.* **688** 687
[15] Sarantopoulos A, Ferreiro-Vila E, Pardo V, Magén C, Aguirre M H and Rivadulla F 2015 *Phys. Rev. Lett.* **115** 166801
[16] Wilk G D, Wallace R M and Anthony J M 2001 *J. Appl. Phys.* **89** 5243
[17] Feng Y, Zhen Y H, Jiang X L, Yang Z R, Qin Z, Yang W J, Qie Y Y and Geng H X 2023 *Ceram. Int.* **49** 14135
[18] Kang R R, Wang Z P, Yang W J, Zhu X P, Shi P, Gao Y F, Mao P, Zhao J T, Zhang L X and Lou X J 2021 *J. Mater. Chem. A* **9** 24387
[19] Dong X Y, Li X, Chen H Y, Dong Q P, Wang J M, Wang X, Pan Y, Chen X L and Zhou H F 2022 *J. Adv. Ceram.* **11** 729
[20] Zhou H Y, Liu X Q, Zhu X L and Chen X M 2018 *J. Am. Ceram. Soc.* **101** 1999
[21] Wang W, Pu Y P, Guo X, Shi R K, Shi Y, Yang M D, Li J W, Peng X and Li Y 2019 *J. Eur. Ceram. Soc.* **39** 5236
[22] Nong P, Pan Y, Dong Q P, Zeng D F, Xu M Z, Wang X, Wang J M, Deng L, Chen X L and Zhou H F 2024 *Electron. Mater. Lett.* **20** 65
[23] Zhang Y B, Liu J K, Bai W F, Zheng P, Wu S T, Li P and Zhai J W 2024 *Chem. Eng. J.* **480** 147974
[24] Guo Y F, Wang J X, Ren Y X, Chen L M and Li J M 2024 *Ceram. Int.* **50** 46729
[25] Qu N, Du H L and Hao X H 2019 *J. Mater. Chem. C* **7** 7993
[26] Dong X Y, Li X, Chen X L, Chen H Y, Sun C C, Shi J P, Pang F H and Zhou H F 2021 *J. Materiomics* **7** 629
[27] Liu J K, Ding Y Q, Li C Y, Bai W F, Zheng P, Wu S T, Zhang J J, Pan Z B and Zhai J W. 2023 *J. Mater. Chem. A* **11** 609
[28] Liu S, Feng W W, Li J H, Tang B, Hu C, Zhong Y, He B and Luo D J 2023 *Chem. Eng. J.* **470** 144086
[29] Liu S, Feng W W, Li J H, He B, Liu M T, Bao Z D, Luo D J and Zhao C C 2022 *J. Eur. Ceram. Soc.* **42** 7430
[30] Liang C, Wang C Y, Cao W J, Zhao H Y, Li F and Wang C C 2023 *J. Adv. Dielectr.* **13** 2242004
[31] Wang C M, Zhang H B, Guo X, Xiao J Z, Zhang X D, Zhang S P, Xie B and Tan H 2024 *J. Chin. Ceram. Soc.* **52** 1240 (in Chinese)
[32] Lai D Y, Yao Z H, You W, Gao B, Guo Q H, Lu P, Ullah A, Hao H, Cao M H and Liu H X 2022 *J. Materiomics* **8** 166
[33] Huan Y, Wei T, Wang X Z, Liu X M, Zhao P Y and Wang X H 2021 *Chem. Eng. J.* **425** 129506
[34] Kang R R, Wang Z P, Yang W J, Zhu X P, Shi P, Gao Y F, Mao P, Zhao J T, Zhang L X and Lou X J 2021 *J. Mater. Chem. A* **9** 24387
[35] Huan Y, Gui D Y, Li C X, Wei T, Wu L Z, Wang X J, Wang X Z and Cheng Z X 2024 *J. Adv. Ceram.* **13** 34
[36] Chen L, Long F X, Qi H, Liu H, Deng S Q and Chen J 2022 *Adv. Funct. Mater.* **32** 2110478
[37] Yao K, Zhou C R, Wang J, Li Q N, Yuan C L, Xu J W, Chen G H and Rao G H 2021 *J. Alloys Compd.* **883** 160855
[38] Fan Y Z, Zhou Z Y, Liang R H and Dong X L 2019 *J. Eur. Ceram. Soc.* **39** 4770
[39] Zhang A Y, Wang T, Liu J X, Chen J H, Chen W and Yang H B 2024 *J. Chin. Ceram. Soc.* **52** 1326 (in Chinese)
[40] Liu J B, Zheng P, Bai W F and Sheng L S 2024 *J. Chin. Ceram. Soc.* **52** 1345 (in Chinese)